Microdroplet based Disposable Sensor Patch for Detection of α-amylase in Human Blood Serum

Mitradip Bhattacharjee [a], Sagnik Middya [b], Pablo Escobedo[a], Joydip Chaudhuri [c], Dipankar Bandyopadhyay* [bc], and Ravinder Dahiya*[a]

[a] Bendable Electronics and Sensing Technologies (BEST) group, University of Glasgow – G12 8QQ, Glasgow, United Kingdom
[b] Centre for Nanotechnology, Indian Institute of Technology Guwahati - 781039, Assam, India
[c] Department of Chemical Engineering, Indian Institute of Technology Guwahati - 781039, Assam, India

*Corresponding author

Emails: dipban@iitg.ac.in; Ravinder.Dahiya@glasgow.ac.uk

Abstract

Concentration of α-amylase in human serum is a key indicator of various pancreatic ailments and an affordable point-of-care detection of this biomarker can benefit millions suffering from these diseases. In view of this situation, we report the development of a flexible patch-sensor, which simply requires a microdroplet of aqueous starch-$FeSO_4$ solution to detect α-amylase in serum. The detection is achieved through the generation of mixing vortices (~12 rpm) inside the droplet with the help of an imposed thermal gradient. Such vortices due to Marangoni and natural convections are found to be strongest at an optimal temperature difference of ~18°C – 23°C across the droplet which in turn facilitate mixing and promote the specific starch-amylase enzymatic reaction. Subsequently, the large (~80%) variation in the electrical resistance across the droplet is correlated to detect the level of the α-amylase in the analyte. Importantly, the sensor can detect even in the limits of 15-110 units/liter. Further, the sensitivity of flexible sensors is ~8.6% higher than the non-flexible one. Interestingly, the sensitivity of the proposed sensor has been nearly three-times than the previously reported optical ones. The results of patch-sensor match very closely with the standard path-lab tests while detecting unknown level of amylase in serum. The prototype has shown significant potential to translate into an affordable device for the real-time detection and easy prognosis of pancreatic disorders.

1. Introduction

Development of affordable and wearable point-of-care (POC) devices for primary healthcare have attracted significant attention in recent years to address the global health challenges (Dahiya 2019; Dahiya et al. 2019; Nayak et al. 2017; Shukla 2018; Tai et al. 2019; Yuan et al. 2019). In particular, there is a significant interest in the design and development of POC devices with disposable sensors to allow frequent measurements (Lin et al. 2017; Nayak et al. 2017) under hygienic conditions (Kafi et al. 2020). In this regard, a wide range of biosensors have been reported recently to evaluate the biomarkers in sweat, tears, urine etc. (Dang et al. 2018; Kafi et al. 2019; Manjakkal et al. 2019; Middya et al. 2019; Thakur et al. 2019) to indicate the potential onset of diseases.

For example, a healthy human serum contains ~25 – 85 U/L (units/liter) α-amylase (endo-1,4-α-d-glucan glucanohydrolase, EC 3.2.1.1) (Wilkins 2009), which helps to hydrolyze the starch into glucose, maltose, and dextrin (Dutta et al. 2016; Gibbs et al. 2015; Mandal et al. 2019; Metzler 2012). An enhanced amylase level indicate the onset of acute pancreatitis, pancreatic cancer, salivary gland infection, bile duct blockage, or gastroenteritis while a reduced level indicate pancreatic or kidney malfunctioning, and toxemia in pregnancy (Wilkins 2009), among others. Importantly, it is very difficult to detect the pancreatic cancer until it reaches an advanced stage. Thus, early detection of α-amylase in saliva, urine, sebum or blood serum and its regular measurement can help prevent several such diseases.

The amylase in human serum is currently detected using spectroscopy (Attia et al. 2014; Gella et al. 1997; van Staden and Mulaudzi 2000), colorimetry (Foo and Bais 1998), fluorometry (Zhang et al. 1990), weight based detection (Sasaki et al. 2008), electrochemical methods (Zajoncová et al. 2004), electromagnetic sensing (Wu et al. 2007) and immunological methods (Svens et al. 1989), as summarized later in the Table 1. Among these, spectrophotometry is considered as the most dependable one (Chavez et al. 1990) even if it is expensive and requires a skilled person for operation and analysis. Considering the linkage of α-amylase with several diseases, a portable POC device can benefit many people and possibly enable self-health management. Importantly, in the recent years, a significant attention has also been paid to self-health management using wearable health monitoring devices (Bandodkar et al. 2019; Dang et al. 2018; Hosseini et al. 2019; Manjakkal et al. 2020; Navaraj et al. 2019; Tai et al. 2019). However, available methods for the detection of α-amylase in human body fluids are unsuitable as wearables or POCs (Luppa et al. 2016).

To this end, we present here a disposable patch-sensor, which needs a microdroplet of aqueous starch-$FeSO_4$ solution to detect α-amylase in blood serum. As a part of the sensing strategy, moderately strong (~12 rpm) mixing vortices are generated inside the microdroplet due to the coupled natural and Marangoni convections by imposing an optimal temperature difference (~18–20°C) across the microdroplet. Subsequently, the variation in the electrical resistance across the salt-laden microdroplet has been correlated to level of α-amylase in human serum. Subsequently, a proof-of-concept POC device, with readout-electronics on a flexible printed circuit board (PCB) has been developed for accurate measurements. The results reported show the significant potential of the prototype to be used as a biomedical device for the real-time detection of pancreatitis at the user's site.

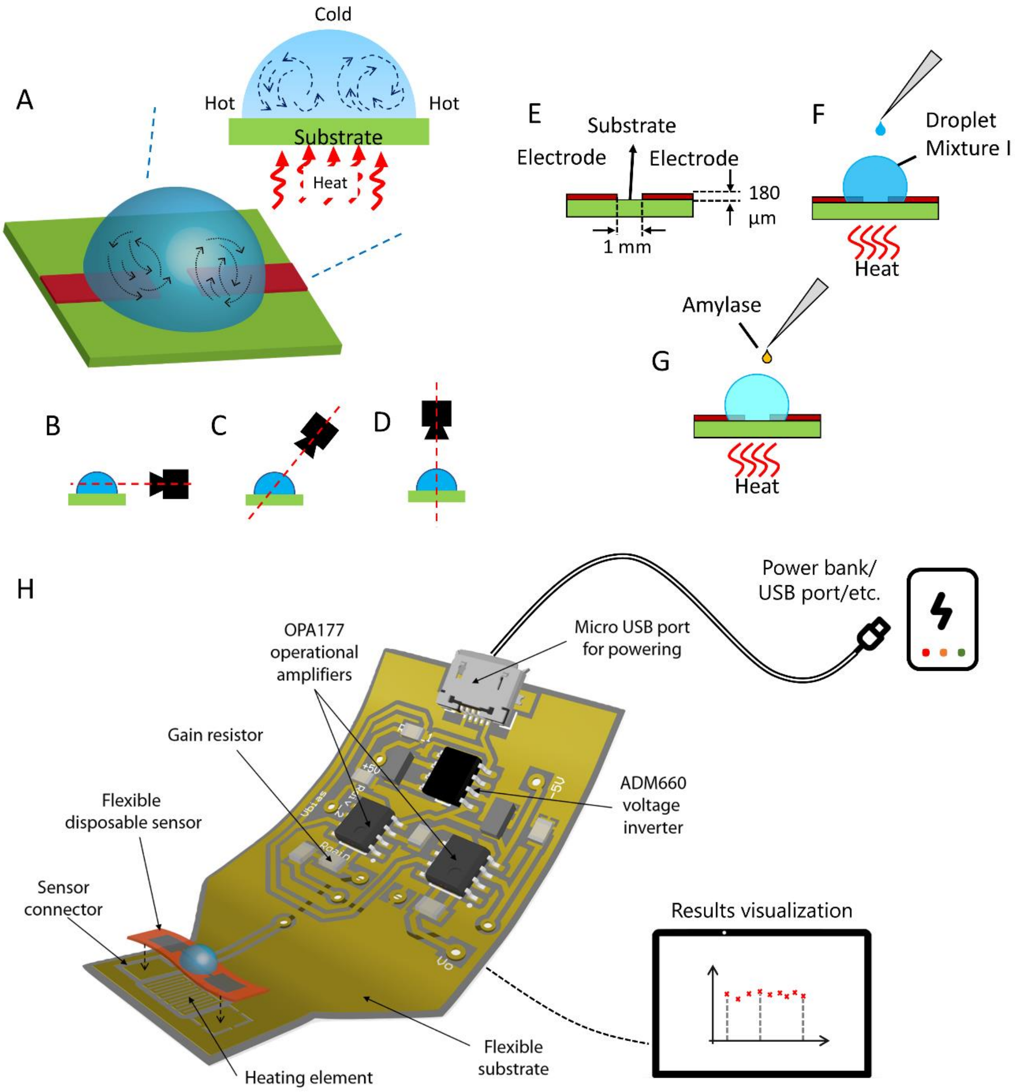

Figure 1: (A) schematic illustration of the experimental set-up. Images (B) and (D) show the placement of digital camera while images (C) and (D) show the position of the thermal imager. Images (E – G) show the experimental procedure and setup. (H) Concept of the device and 3D view of the circuit on flexible substrate for the sensor readout.

The paper has four sections: introduction, experimental section, results and discussions, and conclusions. The result and discussion part are organized systematically with sensing mechanism followed by the origin of sensing described in sections 3.1 and 3.2. The details of flexible sensor experiments are discussed in section 3.3, followed by amylase sensing details in section 3.4, containing the calibration for amylase sensing, unknown sample testing alongside the circuit and system design details.

2. Experimental Section

2.1 Materials

The analytical grade chemicals and materials such as Iron (II) sulfate heptahydrate ($FeSO_4.7H_2O$) and starch (potato starch, procured from Merck) and the enzyme porcine pancreatic amylase (Sigma-Aldrich) were employed in the experiments without further purification. Polyimide flexible sheet, glass slides and commercially available hydrophobic polymer (Scotch 810, acrylic polymer) were used as a substrate for fabrication of the sensors. The Milli-Q grade water was used for cleaning and to prepare the solutions.

2.2 Methods

(i) Characterization of the Rotational Motion: In order to demonstrate the concept, the glass substrate was put on a hot plate (IKA, RCT B S022) and the temperature was varied between (~22^{o}C to ~75^{o}C) to quantify the variation in the rotational motion of the fluid inside the microdroplet, as shown in **Figure 1(A)**. Then a microdroplet of DI water having ~8 mm diameter was dispensed on the glass substrate, as shown in **Figure 1(A).** A digital camera (Sony Handycam) was employed to record the rotational motions inside the microdroplet (positions shown in **Figures 1(B)** and **1(D)**) and a thermal imager (Testo 865) was used to characterize the temperature distribution (positions are shown in the **Figures 1(C)** and **1(D)**). A probe was integrated with the hotplate to measure the temperature of the glass substrate. Different experimental and computational details regarding the rotation are provided in **Figures S2 – S6** in the **Electronic Supporting Information (ESI)**. A similar approach was adopted for flexible substrates. The controlled bending of the polyimide substrate was enacted by fixing them on glass structures with known curvatures. Although the hotplate was for heating, an IR thermometer was used to determine the exact surface temperature. The effects of the bending radius and temperature difference on the rotational motion are described in Section 3.3.

(ii) Experimental Setup for the Sensor: The integration of the sensor started with a glass slide coated with a hydrophobic polymer (Scotch 810, acrylic polymer). Thereafter, a pair of Cu electrodes of diameter 180 μm, with a spacing of 1 mm, was integrated on the polymer-coated glass surface, as shown in **Figure 1(E)**. The flexible sensor was fabricated by depositing metallic electrodes on a polyimide substrate, as described in **Figure S1** of ESI. The electrodes were connected to a digital multimeter (MASTECH M92A(H)), to measure the electrical response. Following this, 10% (w/v) aqueous starch solution and 1M $FeSO_4$ were prepared separately before they were mixed in equal volumes (1:1, v/v) to obtain the 'mixture I'. The substrate integrated with electrodes was placed on a temperature-controlled hotplate. While performing the sensor experiments, initially, a 10 μL drop of the well-stirred mixture I was dispensed symmetrically between the electrodes [**Figure 1(F)**]. The resistance reading in the multimeter stabilized after ~30 s. Thereafter, a microdroplet of porcine pancreatic amylase dissolved in 1x phosphate buffer was dispensed on the starch-salt loaded microdroplet resting on the electrodes [**Figure 1(G)**]. The resistance was then recorded for 1 min at regular time intervals of 2-5 s. The concentration of amylase was varied within 15 and 90 U/L to obtain a calibration for the sensor.

The experiments were repeated for 3 different temperatures, one close to room temperature (26°C), one in the highest activity zone of amylase (40 ± 1^oC), and one high temperature where the evaporation of microdroplet is allowable for these experiments (50 ± 2^oC). The room temperature was recorded as ~22^oC. The individual experiments were performed for 60 - 90 s to avoid resistance fluctuations due to evaporation. Testing of real samples from patients was carried out only at 40^oC, without any pre-treatment. In that case, a 2.5 μL microdroplet of blood serum replaced the amylase solution, which was used for calibration. The testing procedure was kept similar to the one described above for calibration. Finally, the entire sensing setup was translated onto a flexible substrate. It included the flexible sensor as well as the driving and readout electronic circuits, as shown in **Figure 1(H)**.

3. Results and Discussion

3.1 Sensing Mechanism

It may be noted here that the core of the sensing mechanism was attributed to the specific enzymatic reaction between amylase and starch. While the droplet on the flexible patch contained the starch, the analyte dispensed (e.g. amylase in buffer or serum) contained the known or unknown quantity of amylase. In order to promote a homogeneous but fast reaction, the droplet was placed on a heated surface wherein the temperature difference between the base and top of the droplet instigated augmented mixing vortices due to the thermal Marangoni and natural convections, as discussed in the following section. During such a process, the movement of the ions inside the droplet stimulated a reduction in the electrical resistance across the droplet, which was employed as a sensing parameter. The major reason for the increase in the electrical resistance of the droplet with the amylase loading was attributed to the generation of a large number of intermediate ions during the starch-amylase reaction, which has been characterized and discussed in the **Section V** of the **ESI**. Increase in the ions should decrease the resistance across the droplet but, in this case, presence of excess and large number of ions in the system reduce the conductance due to internal collisions of ions and the presence of large molecules of amino acids due to the starch – amylase reactions as described in **Section V** of the **ESI**. We found that the increase in the electrical resistance across the droplet was proportional to the amylase loading in the analyte. In order to amplify such signals, a meagre $FeSO_4$ salt was mixed with the starch solution. In what follows, we elucidate the effects of temperature and other sensing characteristics in a greater detail.

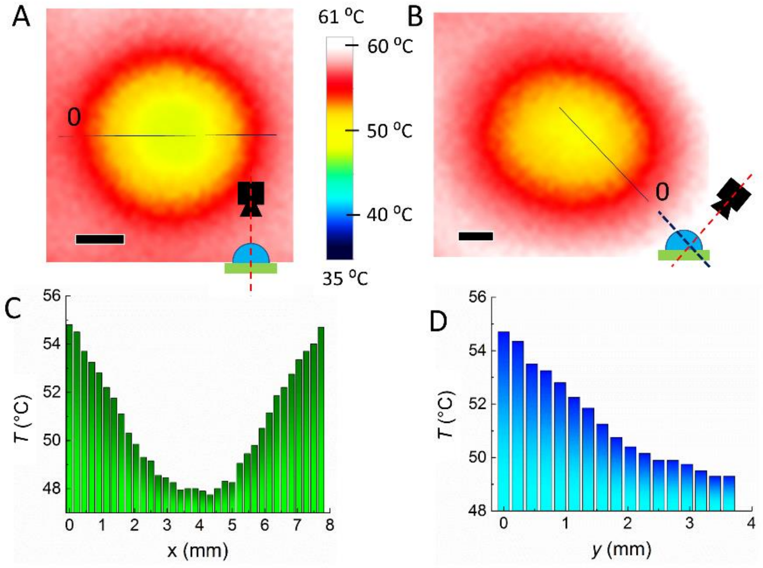

Figure 2: Thermal images (A) and (B) of the microdroplet when the substrate temperature was ~55°C. The bottom right corner in both images show the placement of the thermal imager. (C) and (D) the corresponding temperature distribution plot with respect to distance *d* along *x* and *y* axes, respectively. The scale bars are 2 mm.

The effect of temperature on the microdroplet was studied using digital and thermal imagers. Initially, the experiments were performed on a glass substrate before using the flexible patch. **Figure 1(A)** illustrates the experiment set-up wherein a microdroplet was dispensed on a glass surface before imposing heat from the bottom. In order to track the mixing vortices in the microdroplet a graphite microparticle of ~200 μm was suspended. The rotational motion of the particle in droplet is shown in the **Figure S2** of ESI. A digital camera was used to record the rotational motion, which was further analyzed frame by frame to quantify the rotations. The physics behind these rotational motions have been investigated in detail with the help of a computational analysis.

The thermal characterizations were performed experimentally with an imager. **Figures 2(A)** and **2(B)** show the distribution of temperature across the microdroplet when the thermal imager captured the top and isometric views. **Figures 2(C)** and **2(D)** show the variation of temperature in *x*- and *y*-directions along the cut-planes shown in the thermal images, which were extracted from the images (A) and (B). The "0" on images (A) and (B) of **Figure 2** at one side of the cut-plane indicate, $x = 0$ in the case of image (A) and $y = 0$ in the case of image (B), from which the distance was measured. These images clearly show that the temperature of the microdroplet was higher near the substrate as compared to the free surface of the microdroplet. The actual temperature difference between the substrate and the ambient in the near vicinity (~1 mm) of the microdroplet was measured to be ~ 27°C by placing a temperature sensor. The observed temperature gradient in the thermal image is less (~8°C) due to the optical transparency of the droplet. This temperature difference led to, (i) a surface tension gradient near the air-water interface to facilitate thermal Marangoni flow; and (ii) natural convection due to thermal gradient. In what follows, a brief computational analysis uncovers the physics associated with the interplay of these phenomena and their effects on the sensor performance.

3.2 Origin of Sensing

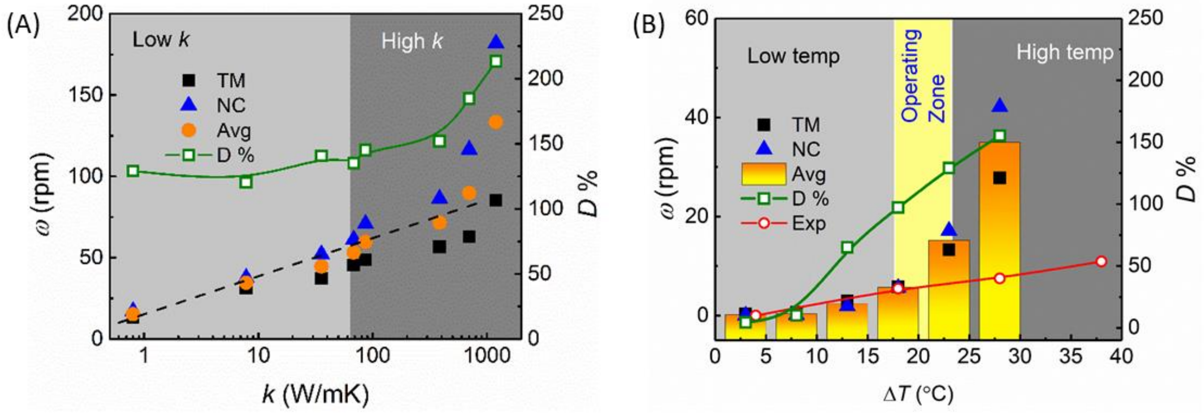

Figure 3: Plot (A) shows the variation of ω with thermal conductivity (k) of the substrate at, $\Delta T = 30$°C. The dotted lines show the slope of the curve. Plot (B) shows the variation of angular velocity (ω) with ΔT for $k = 0.8$ W/mK. The triangular and filled square symbols represent ω

for natural convection (NC) and thermal Marangoni (TM), respectively. The average values of ω (ω_{Avg}) is represented by the bar diagram. The line joining the hollow circular symbols shows the corresponding experimental values of ω at different Δ*T*. The dominance ($D = (NC/TM) \times 100\%$) of TM over NC is illustrated by green line.

The computational analysis uncovered the salient features of the rotational motion and its dependence on parameters like temperature and thermal conductivity of the substrate. The details of the proposed computational model including formulation, boundary conditions, solution methodology, and related equations are discussed in **Section III** of ESI. **Figure 3(A)** shows the effect of thermal conductivity (k) of the solid surface on the average rotational speed (ω_{Avg}, Avg, circle) inside the microdroplet at a fixed substrate temperature (ΔT = 30°C). **Figure 3(A)** suggests that beyond a critical value of $k = k_c$ (~100 W/mK), the rotational motion increased sharply, as indicated by the drastic change in the slope of the plots. The plots also suggest that beyond a k_c the rotation due to natural convection (ω_{NC}, NC, triangle) was higher than the rotation due to thermal Marangoni (ω_{TM}, TM, square) i.e. $\omega_{NC} > \omega_{TM}$, as shown by the demarcated light and dark gray zones. The plot showing the ratio of rotational strength, $R_\omega = (\omega_{NC}/\omega_{TM})$ or dominance $D = (NC/TM) \times 100\%$, indicated the enhanced relative strength of the rotational motions due to NC and TM. Thus, on a glass substrate, with lower k ~0.8 W/mK, the rotational motions originating from the TM and NC could be equally strong and might lead to laminar but strong vortices inside the microdroplet for an efficient mixing.

The **Figure 3(B)** shows the effects Δ*T* on ω_{Avg}, which suggests that, as the temperature gradient across microdroplet increases (from 0.5×10^6 ^{0}C/m to 3×10^6 ^{0}C/m), a higher rotational motion could be observed due to NC and TM for k = 0.8 W/mK. The increase in ω_{TM} and ω_{NC} could be attributed to the higher surface tension and thermal gradients. The ω versus k plots in **Figure 3(A)** suggest that, beyond a critical ΔT_C (~20°C), the rotational motion increased sharply. The computational study suggested that an operating substrate temperature of ~ 40 – 45°C (Δ*T* ~18 – 23°C) could be suitable for the proposed sensor wherein an almost equal strength of TM and NC might lead to the laminar but strong vortices for efficient mixing of analytes. A detailed explanation on these aspects has been provided in **Section III** of ESI. The operating temperature and thermal gradient obtained from the computations were also found to be optimal for the experiments leading to a stable electrical response, minimal evaporation of droplet, optimal enzyme activity, and enzyme stability.

3.3 Experiments with Flexible Sensor

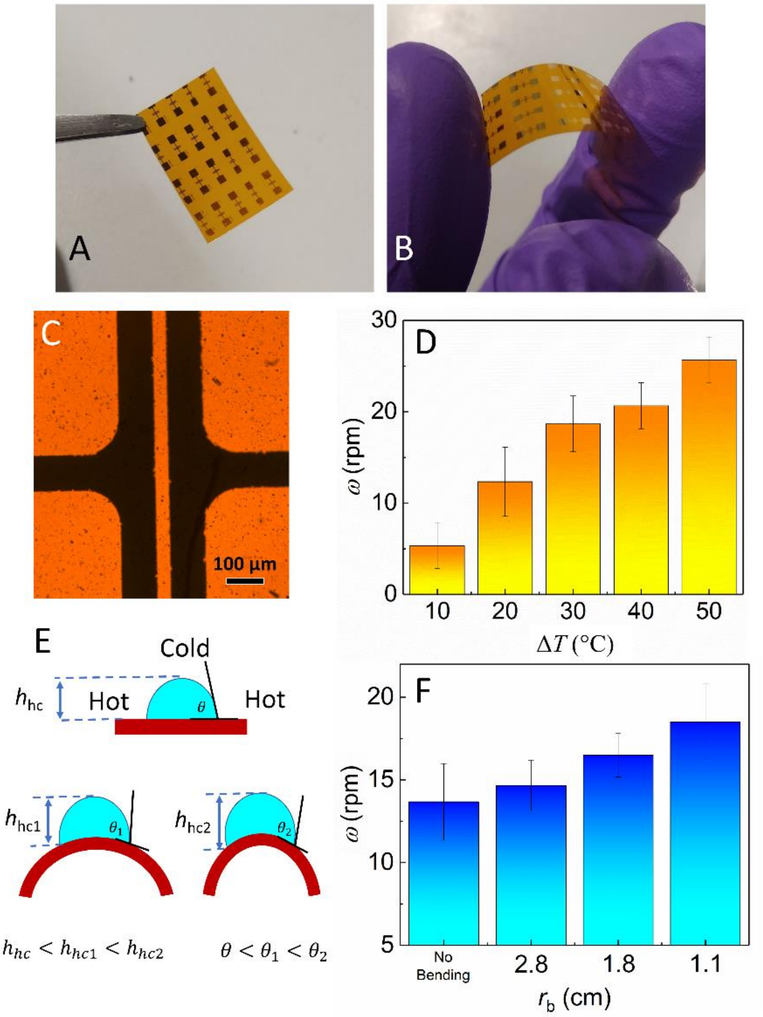

Figure 4: (A-B) the optical images of the flexible sensor. (C) the optical micrograph of Pt electrodes on polyimide substrate. (D) shows the rotation inside the microdroplet for different temperature gradients. (E) schematically shows different bending conditions and the change in height between the hottest and coldest surface (h_{hc}) in the microdroplet. (F) shows how bending effects the rotation inside the microdroplet.

Before performing the experiments on the flexible surfaces, we optimized the droplet volume as well as contact angles following the methods discussed in the **Figures S4** and **S5** of ESI. The experiments for the flexible sensor were done on the polyimide substrate because of its surface energy, thermal stability and conductivity (~1.2 W/mK). **Figures 4(A)** and **(B)** show the images of sensor-array-electrodes on polyimide. **Figure 4(C)** shows the microscope image of the electrodes. The response of the flexible sensors patch was identified by performing a series of experiments at different temperatures and noting ω, as reported in **Figure 4(D)**. It was observed that ω was almost twice the sensors on the glass (~0.8 W/mK) owing to the higher thermal conductivity of polyimide. In a way, a combined effect of higher thermal conductivity and lower thickness (~60 μm) of polymer facilitated a higher ω in the microdroplet. The influence of substrate bending on the rotation inside the microdroplet was also determined experimentally for three bending radii of 1.1, 1.8, and 2.8 cm, as shown in the **Figure 4(E)**. It was observed that the rotation inside the microdroplet increased with bending of the substrate (decrease in bending radius, r_b, **Figure 4(F)**). Such an observation could be attributed to the increase in the hot-cold barrier height (h_{hc}) – the maximum distance between the hottest and coldest part of droplet and contact line.

The h_{hc} was higher in bending conditions compared to a flat surface. Moreover, the effective contact angle (θ) was also higher in bending conditions, as shown in **Figure S6**. However, this also promoted the evaporation of fluid at higher temperatures and thus temperatures beyond 60ºC was not suitable for these measurements. For a smaller bending (i.e. higher r_b) the mixing vortices was stable. Thus, the electrical measurements were carried out for a droplet of diameter ~3 - 4 mm to minimize the disturbance upon bending. This was in line with the inference from the computational study (**Figure S5**), which revealed an optimal radius $r = 0.1 - 0.4$ cm for this operation.

3.4 Sensor Fabrication and Performance

The experimental set-up for the sensing is illustrated in **Figure 5(A)**. In order to identify the optimal operating temperature, three substrate temperatures i.e. 26, 40, and 50°C were fixed. The experiments were initially carried out on the glass substrate. After 10 μL of mixture I is dispensed on the electrodes, the electrical resistance across the droplet (R_D) varied with time. **Figure S7(A)** in **ESI** shows the variation of R_D with time (t) for amylase concentration, C_A = 20 U/L and a substrate temperature of 26°C. Following the injection of the test sample at $t = 0$, there were two distinct phases in the variation of R_D, (i) unstable phase – when the rotational motions inside the microdroplet due to TM and NC were established leading to a rapid increase in R_D, and (ii) pre-saturation phase – when vortices became stable and R_D increased to reach a plateau. The boundary between the two phases was conveniently decided at $t = 10$ s from general observations across all measurements. **Figure S7(B)** shows the resistance response of the sensor with different concentration of amylase.

The α-amylase selectively hydrolyses starch into maltose and other small MW carbohydrates (Butterworth et al. 2011; Mishra et al. 2002; Moore et al. 2015). According to the prior art (Chiba 1997; Kaneko et al. 1999; Kempton and Withers 1992), the starch-amylase reaction often leads to an excess of intermediate protonated carboxyl and oxocarbenium ions, which can be the major reason behind the observed increase in R_D. Presence of relatively bulkier ions, restricts the overall ion movement inside the droplet and hence the resistance across the droplet increases. Apart from this, the Fe^{2+} ions interacts with negatively charged amino acid residues, which further helps to restrict ions movement and contribute to the increase in R_D (Chiba 1997; Kaneko et al. 1999; Kempton and Withers 1992). A detailed explanation regarding this has been provided in **Section V** of the **ESI**.

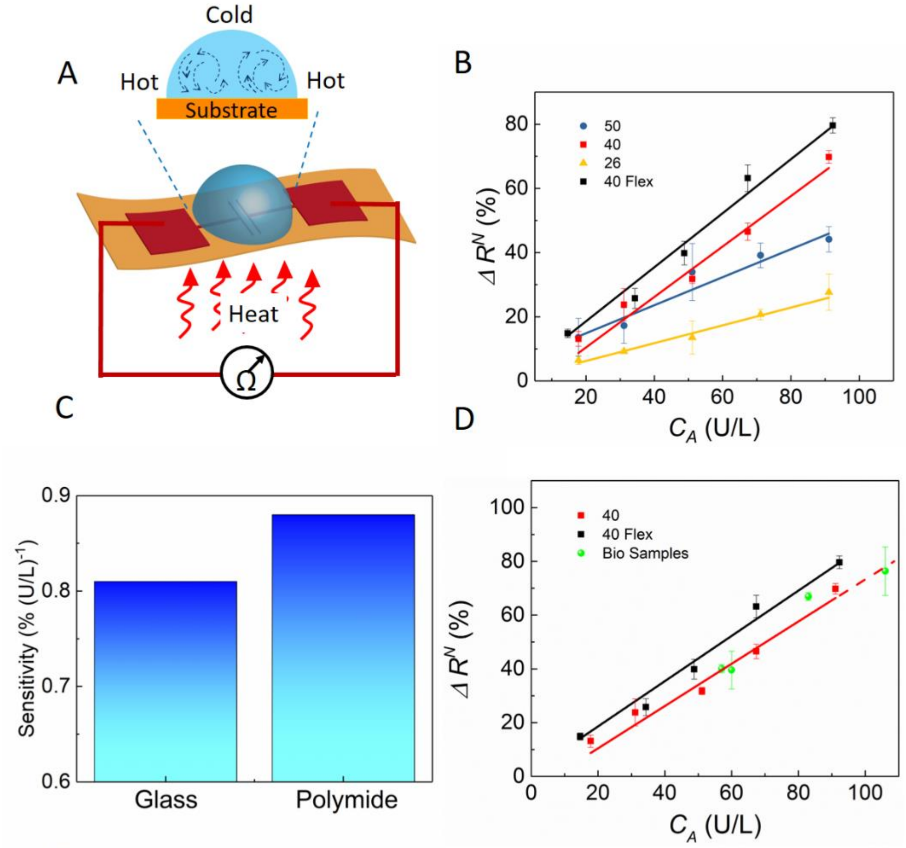

E

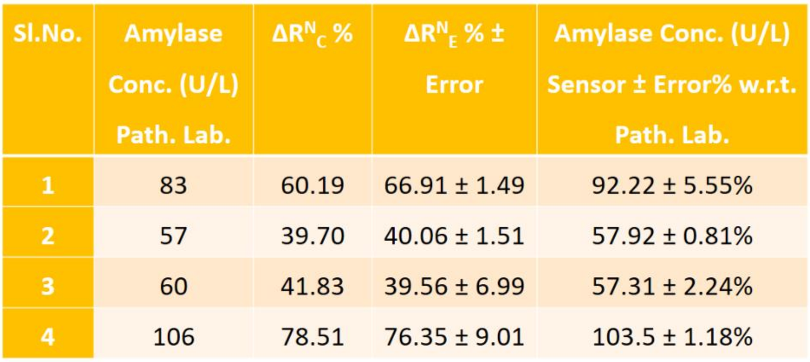

Sl.No.	Amylase Conc. (U/L) Path. Lab.	ΔR^N_C %	ΔR^N_E % ± Error	Amylase Conc. (U/L) Sensor ± Error% w.r.t. Path. Lab.
1	83	60.19	66.91 ± 1.49	92.22 ± 5.55%
2	57	39.70	40.06 ± 1.51	57.92 ± 0.81%
3	60	41.83	39.56 ± 6.99	57.31 ± 2.24%
4	106	78.51	76.35 ± 9.01	103.5 ± 1.18%

Figure 5: (A) Schematic of the experimental set-up to measure α-amylase level in test sample. (B) shows the response for different concentration of α-amylase at 3 different substrate temperatures (glass, 50ºC, 40ºC, and 26ºC) and for polyimide substrate at 40ºC (40 Flex). (C)

shows the response of the sensor for glass (40) and polyimide (40 Flex) substrate at 40ºC. (D) shows the comparison of serum (scattered points) with the calibration curves (continuous). The table (E) shows the comparison between the results obtained from the proposed sensor and from a standard pathological laboratory (path. lab.). Here, ΔR^{N}_{C} and ΔR^{N}_{E} represent the sensor response from calibration and experiments, respectively.

Naturally, a higher change i.e. increase in R_D could be expected for a higher concentration of amylase. Raman spectroscopy in the **Figure S7(C)** of ESI helped in elucidating the molecular mechanisms of the starch-amylase reaction. **Figure S7(D)** illustrates that control experiments in the absence of starch or amylase showed significantly lower response as compared to when both were present. Similarly, experiments were also performed without heat. It was observed that without heat the response of the sensor was rather random, as illustrated in **Figure S7(E)**. Further details on the temporal response of sensor, control experiments, and reaction mechanism are provided in **Section V** of the ESI.

The sensor response was quantified as normalized variation in R_D ($\Delta R^N = (R_t - R_0)/R_0$), where R_t and R_0 denote the resistances at t = 30 s and 10 s, respectively. The interval of measurement was chosen since it avoided the unstable phase, evaporation, and saturation. **Figure 5(B)** shows that a higher ΔR^N was observed for a higher concentration of amylase irrespective of the temperature. The best response was found to be at the temperature of ~40°C (ΔT ~ 18ºC), as suggested by the computational analysis in **Figure 3(B)**. Moreover, the free α-amylase shows the highest activity at the temperature range of 37–42°C. Following this, the flexible polyimide system was also tested for the detection of amylase at ~40°C (ΔT ~ 18ºC). The response was recorded for various concentrations of amylase (C_A) and the flexible sensor showed a better response. It was found that the sensitivity of the polyimide system was ~8.6% higher than that of the glass substrate, as illustrated in **Figure 5(C).** The higher circulation and compact electrode in the polyimide system facilitated the amylase-starch reaction and provided a more stable and better response.

Experiments with human serums showed a close match with the calibration curve. The serum tests were carried out under the supervision of medical personal in a diagnostic center. The amylase in serum was first measured using Dimension RxL Max Integrated Chemistry System, SIEMENS. Thereafter, the bio-samples were tested in the proposed sensing arrangement at 40°C (ΔT ~ 18ºC), as shown by scattered points in **Figure 5(D)**. The results for the bio-samples were also compared with the tests conducted in a path-lab, as shown in **Figure 5(E)**. The calibrated response in **Figure 5(D)** is denoted as ΔR^{N}_{C} while ΔR^{N}_{E} refers to the response obtained when the bio-samples were measured with the proposed sensor. Column V shows the C_A values for the measured ΔR^N_E including errors with respect to the path-lab readings in column II. The table suggests that the C_A corresponding to ΔR^N_E (column V) match closely with the actual results of path-lab.

Table 1: Shows a comparison between this work with other reported in the literature

Sl. No.	Type	Avg. Sensitivity	Range (U/L)	POC Enabl.	Cost	Specific Sensor	Ref.
1	Spectroscopy	-	-	No	High	No	Attia et. al. 2014
2	Electrochemical	0.3 nA/mMol	>50	No	High	Yes	Zajoncová et. al. 2004
3	Fluorometry	-	<400	No	High	No	Zhang et. al. 1990
4	Weight based	0.88 ng/cm^2.min	0. 1-10^3	No	High	Yes	Sasaki et. al. 2008
5	Colorimetry	0.27 %(U/L)$^{-1}$	10-110	Yes	Affordable	Yes	Dutta et. al. 2016
6	Electrical	0.85 %(U/L)$^{-1}$	25-100	Yes	Affordable	Yes	Mandal et. al. 2019
7	Immunological	-	4-1000	No	High	No	Svens et. al. 1989
8	Magnetic	2.25 Hz(U/ml)$^{-1}$	(75-125).10^3	No	High	Yes	Wu et. al. 2007
9	Electrical	-	80-8000	No	-	Yes	Gibbs et. al. 2015
10	**Microdroplet**	**0.88 %(U/L)$^{-1}$**	**15-110**	**Yes**	**Affordable**	**Yes**	**This work**

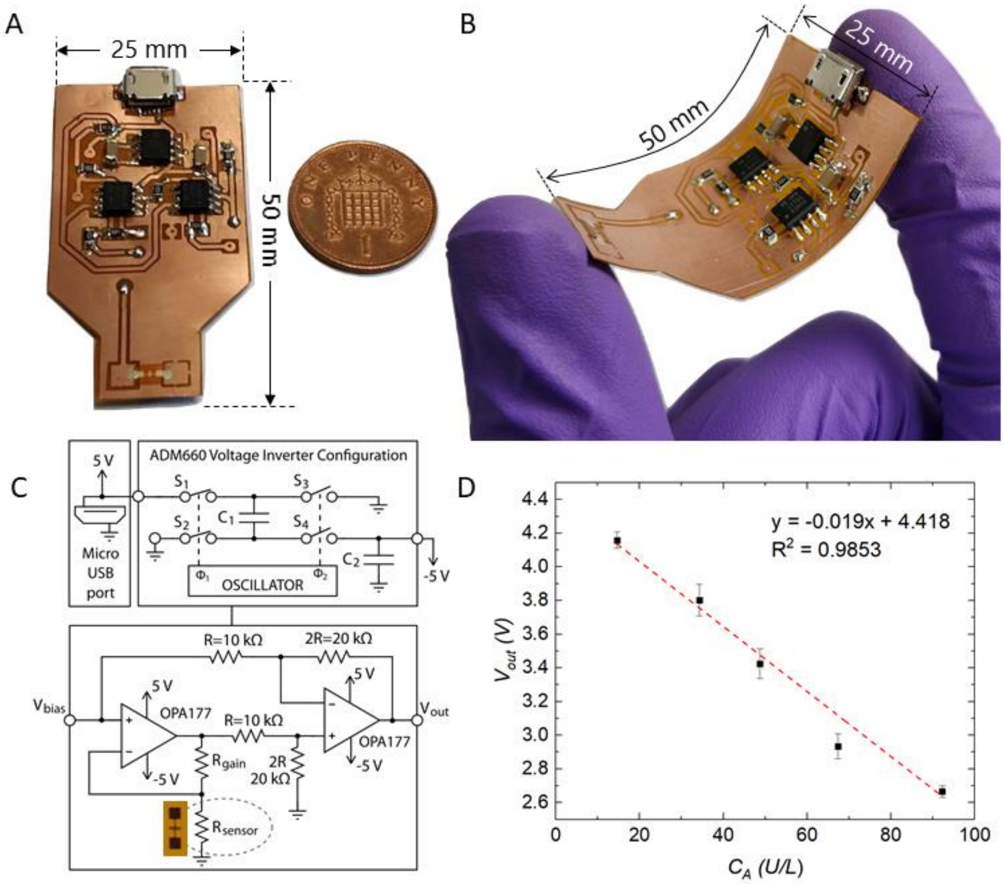

Figure 6: (A, B) Photograph of the flexible readout circuit with sensor attached. (C) Schematic diagram of the analogue front-end implementation consisting of a constant voltage with offset and amplification circuit. (D) Calibration curve of the output voltage of the readout circuit as a function of α-amylase concentration.

Table 1 shows a comparison of the performance of the proposed sensor with those reported previously. The data suggest that the sensitivity of the proposed sensor was nearly thrice than a reported optical sensor. Further, **Figure S8** in the ESI shows that the sensor was quite stable and the flexible patch was low-cost, disposable, and reusable for the experiments. A stable response from the flexible sensor patch was observed even after 4 months of fabrication, as shown in **Figure S9** in the ESI. Further, a readout circuit was designed and fabricated for the sensor to accurately detect the concentration of amylase.

Figures 6(A) and **(B)** show a photograph of the prototype on a flexible FR4 substrate. As a resistive device, the proposed sensor required an appropriate excitation supply to measure the changes in resistance with α-amylase loading. Among the different implementations for the analogue front-end, a constant voltage excitation circuit with offset compensation and amplification was designed (**Figure 6(C)**). This circuit enhanced accuracy at the cost of increased design complexity when compared to other alternatives such as voltage dividers or constant voltage driving circuits without amplification. The sensor conditioning circuit consisted of two precision operational amplifiers OPA177 (Texas Instruments, Texas, USA), which have very low offset voltage (25 µV maximum) and drift (0.3µV/°C). Since such devices were dual supply op-amps, a supply voltage of ±5 V was required for their correct operation. Therefore, a voltage inverter based on the ADM660 integrated circuit (Analog Devices, USA) was designed to obtain the negative voltage of –5V from the positive supply. This chip was chosen due to its low quiescent current, 600 µA, and the easy inverter configuration in which only two external capacitors were required. The positive supply of +5 V could be obtained through a micro USB connector attached to the circuit, as shown in **Figure 6(A)**. The bias voltage was obtained from the same source using a resistor-based voltage divider. The resulting output voltage (V_{out}) had a simple and direct relationship to the resistive sensor value as,

$$V_{out} = 2V_{bias}\left(\frac{R_{gain}}{R_{sensor}}\right)$$

where V_{bias} = 0.5 V to keep the sensor under appropriate biasing conditions and to avoid any noise due to electrolysis. The value of R_{gain} was kept 708 kΩ to maximize the output voltage range while keeping the values within the input common-mode voltage. **Figure 6(D)** shows the calibration curve where the output voltage followed a linear trend from 4.16 V down to 2.67 V when the concentration of α-amylase changes from 14.6 U/L up to 92.2 U/L. This means a voltage change of 1.5 V between both limits.

4. Conclusions

We exploit the thermal gradient imposed natural and Marangoni convections to induce mixing vortices inside a microdroplet. The vortices facilitated the specific enzymatic reaction between α-amylase and starch which in turn was employed to develop a microdroplet patch-sensor targeting POC applications. The thermal gradient at the base of the droplet engendered a rotational motion of ~12 rpm when the substrate temperature was 40°C. A computational study uncovered that the variation in interfacial tension and density across the microdroplet due to variation of temperature generated the mixing vortices. The contribution from Marangoni motion was dominant at smaller temperature gradients (ΔT = 10°C) whereas, at higher temperature gradients (ΔT = 50°C), the natural convection was dominant. The temperature ranges between 40ºC – 45°C (ΔT ~ 18ºC - 23ºC) was found to be optimal for the sensing operation. The microdroplet sensor was fabricated on both rigid and flexible substrates, which has shown the potential to detect α-amylase in blood serum in the range of 15 –110 U/L. It was observed that the sensitivity of the disposable flexible sensor was ~8.6% higher than that of the non-flexible glass-based sensor. The sensor patch was found to be stable for more than 4 months. Further, a comparison with other existing sensors uncovered the superiority of the proposed microdroplet patch-sensor. Finally, a flexible PCB was developed to accurately measure the level of α-amylase in serum and demonstrate the potential of the prototype to translate into an easy to use POC device. As a future scope, integration of a heating element on the flexible PCB can convert the prototype into a real-time POC device. The results reported suggest that the prototype can be employed for real-time detection and early diagnosis of pancreatic disorders.

AUTHOR INFORMATION

Notes

The authors declare no conflict of interest.

ACKNOWLEDGEMENT

This work was supported in part by Engineering and Physical Sciences Research Council (EPSRC) Engineering Fellowship for Growth neuPRINTSKIN (EP/R029644/1 and EP/M002527/1) and North West Centre for Advanced Manufacturing (NW CAM) project supported by the European Union’s INTERREG VA Programme (H2020-Intereg-IVA5055), managed by the Special EU Programmes Body (SEUPB) and Government of India through MHRD-IMPRINT Grant No. 8058 and MeitY grant no. 5(9)/2012-NANO.

REFERENCES

Attia, M.S., Zoulghena, H., Abdel-Mottaleb, M.S.A., 2014. Analyst 139(4), 793-800.

Bandodkar, A.J., Choi, J., Lee, S.P., Jeang, W.J., Agyare, P., Gutruf, P., Wang, S., Sponenburg, R.A., Reeder, J.T., Schon, S., Ray, T.R., Chen, S., Mehta, S., Ruiz, S., Rogers, J.A., 2019. Advanced Materials 31(32), 1902109.

Butterworth, P.J., Warren, F.J., Ellis, P.R., 2011. Starch - Stärke 63(7), 395-405.

Chavez, R.G., David, H., Metzner, E.K., Sigler, G.F., Winn-Deen, E.S., 1990. United States.

Chiba, S., 1997. Bioscience, Biotechnology, and Biochemistry 61(8), 1233-1239.

Dahiya, R., 2019. Proceedings of the IEEE 107(2), 247-252.

Dahiya, R., Akinwande, D., Chang, J.S., 2019. Proceedings of the IEEE 107(10), 2011-2015.

Dang, W., Manjakkal, L., Navaraj, W.T., Lorenzelli, L., Vinciguerra, V., Dahiya, R., 2018. Biosensors and Bioelectronics 107, 192-202.

Dutta, S., Mandal, N., Bandyopadhyay, D., 2016. Biosensors and Bioelectronics 78, 447-453.

Foo, A.Y., Bais, R., 1998. Clinica Chimica Acta 272(2), 137-147.

Gella, F.J., Gubern, G., Vidal, R., Canalias, F., 1997. Clinica Chimica Acta 259(1), 147-160.

Gibbs, M.J., Biela, A., Krause, S., 2015. Biosensors and Bioelectronics 67, 540-545.

Hosseini, E.S., Bhattacharjee, M., Manjakkal, L., Dahiya, R., 2019. In: Stuart, S., Godfrey , A. (Eds.), From A to Z: Wearables in modern medicine. Elsevier.

Kafi, M.A., Paul, A., Vilouras, A., Dahiya, R., 2020. Biosensors and Bioelectronics 147, 111781.

Kafi, M.A., Paul, A., Vilouras, A., Hosseini, E.S., Dahiya, R.S., 2019. IEEE Sensors Journal, 1-1.

Kaneko, H., Kuriki, T., Okada, S., 1999. Journal of Applied Glycoscience 46(2), 187-197.

Kempton, J.B., Withers, S.G., 1992. Biochemistry 31(41), 9961-9969.

Lin, H.-Y., Huang, C.-H., Park, J., Pathania, D., Castro, C.M., Fasano, A., Weissleder, R., Lee, H., 2017. ACS Nano 11(10), 10062-10069.

Luppa, P.B., Bietenbeck, A., Beaudoin, C., Giannetti, A., 2016. Biotechnology Advances 34(3), 139-160.

Mandal, N., Bhattacharjee, M., Chattopadhyay, A., Bandyopadhyay, D., 2019. Biosensors and Bioelectronics 124-125, 75-81.

Manjakkal, L., Dang, W., Yogeswaran, N., Dahiya, R., 2019. Biosensors 9(1), 14.

Manjakkal, L., Pullanchiyodan, A., Yogeswaran, N., Hosseini, E.S., Dahiya, R., 2020. Advanced Materials.

Metzler, D., 2012. Elsevier Science, New York, US.

Middya, S., Bhattacharjee, M., Bandyopadhyay, D., 2019. Nanotechnology 30(14), 145502.

Mishra, P.J., Ragunath, C., Ramasubbu, N., 2002. Biochemical and Biophysical Research Communications 292(2), 468-473.

Moore, S.A., Ai, Y., Chang, F., Jane, J.-l., 2015. Carbohydrate Polymers 115, 465-471.

Navaraj, W., Smith, C., Dahiya, R., 2019. In: Parlak, O., Salleo, A., Turner, A.P.F. (Eds.), Wearable Bioelectronics, pp. 133-178. Elsevier.

Nayak, S., Blumenfeld, N.R., Laksanasopin, T., Sia, S.K., 2017. Analytical chemistry 89(1), 102-123.

Sasaki, T., Noel, T.R., Ring, S.G., 2008. Journal of Agricultural and Food Chemistry 56(3), 1091-1096.

Shukla, A.Y., 2018. The Journal of mHealth 1(1), P1-P27.

Svens, E., Kapyaho, K., Tanner, P., Weber, T.H., 1989. Clinical Chemistry 35(4), 662-664.

Tai, L.-C., Liaw, T.S., Lin, Y., Nyein, H.Y.Y., Bariya, M., Ji, W., Hettick, M., Zhao, C., Zhao, J., Hou, L., Yuan, Z., Fan, Z., Javey, A., 2019. Nano Letters 19(9), 6346-6351.

Thakur, S., Bhattacharjee, M., Dasmahapatra, A.K., Bandyopadhyay, D., 2019. ACS Sustainable Chemistry & Engineering 7(14), 12069-12082.

van Staden, J.F., Mulaudzi, L.V., 2000. Analytica Chimica Acta 421(1), 19-25.

Wilkins, L.W., 2009. Lippincott Williams & Wilkins.

Wu, S., Zhu, Y., Cai, Q., Zeng, K., Grimes, C.A., 2007. Sensors and Actuators B: Chemical 121(2), 476-481.

Yuan, Z., Hou, L., Bariya, M., Nyein, H.Y.Y., Tai, L.-C., Ji, W., Li, L., Javey, A., 2019. Lab on a Chip 19(19), 3179-3189.

Zajoncová, L., Jílek, M., Beranová, V., Peč, P., 2004. Biosensors and Bioelectronics 20(2), 240-245.

Zhang, Z., Seitz, W.R., O'Connell, K., 1990. Analytica Chimica Acta 236, 251-256.